Variability of Internally Generated Turbulence in an Estuary, from 100 Days of Continuous Observations

Philip M. Orton[a*] and Martin Visbeck[a,b]

[a] Lamont-Doherty Earth Observatory of Columbia University, 61 Route 9W, Palisades, NY 10964

[b] Leibniz-Institut fuer Meereswissenschaften (IFM-GEOMAR), Duesternbrooker Weg 20, D-24105 Kiel, Germany

* Corresponding author: orton@ldeo.columbia.edu

Abstract

We present detailed observations of internally generated turbulence in a sheared, stratified natural flow, as well as an analysis of the external factors leading to its generation and temporal variability. Multi-month time series of vertical profiles of velocity and acoustic backscatter (0.5 Hz) and turbulence parameters were collected with two moored acoustic Doppler current profilers in the Hudson River estuary, and estuary-long transects of water density were collected thirty times. ADCP backscatter is used for visualization of coherent turbulent structures and evaluation of surface wave biases to the turbulence measurements. Benefits of the continuous long-term turbulence record include our capturing: (1) the seasonality of turbulence due to changing riverflow, (2) hysteresis in stratification and turbulence over the fortnightly cycle of tidal range, and (3) intermittent events such as breaking internal waves. Internal mixing layers (IMLs) are defined as turbulent regions above the logarithmic velocity layer, and the bottom boundary layer (BBL) is defined as the continuously turbulent range of heights above the bed. A cross-correlation analysis reveals how IML and BBL turbulence vary with stratification and external forcing from tidal range, river flow, and winds. Turbulence in both layers is maximal at spring tide and minimal when most stratified, with one exception – IML turbulence at a site with changing channel depth and width is maximal at times of maximum stratification and freshwater input.

Keywords: USA; New York; Hudson River; vertical mixing; turbulence measurement; estuary; Reynolds stresses, acoustic Doppler current profiler

1. Introduction

Vertical turbulent mixing is a primary determinant of transport in all but the most stratified estuaries, with vigorous turbulence promoting retention, and stratification promoting along-channel dispersion. A fundamental problem with numerical hydrodynamic modeling, however, is the incomplete representation of the nonlinear physics of turbulence. Numerical models require turbulence parameterizations because of computer processing constraints, but studies have shown that the many available schemes do not reflect turbulence variability over a wide range of stratification (e.g. Stacey et al., 1999b; Sharples, 2005).

An important goal, if we are to understand estuarine transport dynamics and improve numerical models, is to obtain a more complete database of field observations of turbulence parameters. Whereas turbulence parameterizations can be indirectly tested by the ability of a model to reproduce the mean flow or salinity field, a more critical test is the ability to describe the depth dependence and time evolution of turbulence (Simpson et al., 1996). Studies have clarified the important role of bottom boundary layer (BBL) turbulence in estuaries (e.g. Geyer et al., 2000; Chant et al., 2007), a process that is well-predicted by model parameterizations.

It has long been known that along-estuary bathymetric variations or the presence of strong stratification and shear can cause "interfacial" turbulence (e.g. internal wave breaking) at a sharp estuarine pycnocline (Geyer and Smith, 1987; Peters, 1999; Chant and Wilson, 2000; Stenstrom, 2004). Furthermore, turbulence above the logarithmic velocity layer is generated by local shear instabilities and modified by stratification (if present), not directly generated by bottom friction (Peters and Bokhorst, 2000). These forms of turbulence, hereafter referred to as internal mixing layer (IML) turbulence (**Fig. 1**), have higher mixing efficiency than BBL turbulence due to the stronger vertical gradients in water properties (Lewis, 1996; Rippeth, 2005). It has been

acknowledged that IML turbulence is a more difficult modeling task (Simpson et al., 1996; Sharples, 2005). However, few full water column studies of turbulence have been carried out because methods for observing a full vertical profile of turbulence parameters have until recently required costly ship-based measurements.

Recent advances in acoustic Doppler current profiler (ADCP) techniques for observing turbulence are now enabling researchers to measure turbulence parameters autonomously for multiple days and through most of the water column (Stacey et al., 1999a; Lu and Lueck, 1999; Gargett et al., 2004). The result is an increasing number of studies of ephemeral turbulence events at the ocean's margins, including tidal bores (Simpson et al., 2004), storm-driven Langmuir supercells (Gargett et al., 2004), and dense deepwater gravity currents (Peters et al., 2006).

Here, we contrast the variability of IML and BBL turbulence in the Hudson River estuary using two continuous 100+ day ADCP velocity, turbulent stress, and acoustic backscatter datasets and 30 along-estuary CTD transects. Although our observations span time scales from seconds to seasons, in this paper we primarily focus on the sub-tidal signals. A cross-correlation analysis reveals how IML and BBL turbulence vary with stratification and external forcing from tidal range, river flow, and winds. Significant correlations are discussed and in most cases matched with physical explanations. We synthesize these results by discussing the broader implications of IML turbulence variability in terms of estuarine modeling, circulation, fine sediment and pollutant transports, and air-water gas exchange.

2. Field Program and Data Processing

Ongoing monthly along channel CTD transects have now been run 30 times from The Battery (km 0) to Green Island, NY (km 243) since 2001, with the aid of the Hudson Riverkeeper. A Seabird SBE-19+ CTD is used for profiling along the estuary's thalweg (deepest cross-sectional location) to best track the salt intrusion, and data are bin-averaged to 0.5 m vertical resolution. Acoustic Doppler current profiler (ADCP) tripods were deployed on the bed of the Hudson (**Fig. 2**) near Piermont (Site B; 3/24/04 - 7/12/04) and at the Hudson Highlands entrance sill in northern Haverstraw Bay (Site C; 3/24/04 - 7/3/04). Each held a Teledyne-RDI (TRDI) ADCP (Workhorse Monitor, 1200kHz) facing upward to monitor water velocity and acoustic backscatter through the water column. Continuous density estimates are available for the Site B tripod (at z = 0.5 m), surface water 6 km southward (USGS, unpublished data at Hastings-on-Hudson, 2004), and at surface and bottom water C-T sensors about 6 km south and 12 km north of Site C (R. Geyer, unpublished data, 2004).

Ambient conditions during the ADCP deployments covered nearly the complete range of riverflow, tidal and wind forcing that act upon the Hudson (**Fig. 3**). Freshwater input (Q) at the head of the tidal river (Green Island dam) peaked at 1800 $m^3 s^{-1}$ (twice), and bottomed out at 130 $m^3 s^{-1}$. The 1980-2004 Q data show a mean of 400 $m^3 s^{-1}$, and in a typical year, Q varies by a factor of 25, with means for annual minimum and maximum of 90 $m^3 s^{-1}$ and 2340 $m^3 s^{-1}$ (USGS, 2006). Water depth from Site B shows significant fortnightly variability in tidal range, including a minimal apogean neap tide. A continuous wavelet transform (CWT) was used to quantify tidal forcing, decomposing these data into semi-diurnal (D2) and diurnal (D1) species, as well as several overtide and sub-tidal species. The fundamental benefit of the CWT over traditional harmonic analysis is that it resolves the time-variation of frequency content, with no assumption of stationarity (Flinchem and Jay, 2000). Wind stress was computed from wind observations off the

mouth of the Hudson in New York Bight (NOAA, 2006) using a quadratic drag law $\tau_w = \rho_{air} C_d U_w^2$. Here, the air density ρ_{air} is 1.2 kg m^{-3} and the sea surface drag coefficient C_d is 0.001 (Large and Pond, 1981). The 8-hour average wind speed was as high as 20 m s^{-1} in one isolated stormy period (τ_w = 0.45 Pa), but more typical wind maxima were 10-13 m s^{-1} (τ_w = 0.1-0.2 Pa).

2.1 ADCP turbulence sampling and processing

ADCP sampling characteristics and processing were optimized for two months of turbulence sampling per deployment, given battery (3-57V D-cell stacks) and memory (2 GB) limitations. TRDI's rapid sampling mode-12 was used to record one ensemble average every 2 s, an average of 15 sub-pings that were collected over about ~0.6 s (40 ms intervals). The vertical cell size was 0.5 m, and the resulting manufacturer estimate of velocity standard error is 1.5 cm s^{-1}. Velocity and turbulent stress data were rotated from the earth reference frame into the direction of maximum near-bed velocity variance, to an along-stream (x) and across-stream (y) orthogonal reference frame. Data from the upper 6% of the water column were omitted, a standard procedure required because of acoustic side-lobe reflections off the sea surface, so data is available from 1.75 m above the bed to ~1 m below the sea surface.

ADCP data were used to compute 20-minute averages of the along- and across-stream vertical turbulent stress (τ_{xz}, τ_{yz}), turbulent kinetic energy production (P), and eddy viscosity (A_z) with 5-minute increments through time (75% overlap). Researchers have developed a methodology called the “variance method” for an ADCP, to measure these turbulence parameters with minimal spatial averaging. Assuming that instrument tilts are negligible (they were below 2° at all times), and that

second-order moments of the flow (e.g. $\overline{u'^2}, \overline{u'w'}$) are horizontally homogeneous between beams, we compute turbulent stress (Lu and Lueck, 1999; Stacey et al., 1999a):

$$\tau_{xz} = -\rho\overline{u'w'} = \frac{\rho\left(\overline{b_4'^2} - \overline{b_3'^2}\right)}{4\sin\theta\cos\theta} \qquad \tau_{yz} = -\rho\overline{v'w'} = \frac{\rho\left(\overline{b_2'^2} - \overline{b_1'^2}\right)}{4\sin\theta\cos\theta} \qquad (1, 2)$$

Here, b_i are along-beam velocities (i = 1,2,3,4), ρ is the water density, and θ is the angle each beam makes with the vertical axis. Prior studies comparing ADCP turbulence measurements to those from shear microstructure or bottom-mounted acoustic Doppler velocimeters have shown good correspondence (Lu et al., 2000; Rippeth et al., 2003; Simpson et al., 2005). Our stress noise floor for periods with weak turbulence, based on methods described in Williams and Simpson (2004), is σ_τ = 0.015 Pa.

Where there are non-zero stresses, kinetic energy of the mean flow is converted into small-scale turbulence, an energy flux measured by our ADCP as shear production of turbulent kinetic energy (P). This is computed directly from these stresses and the mean shear (Rippeth et al., 2002):

$$P = \tau_{xz}\frac{\partial\bar{u}}{\partial z} + \tau_{yz}\frac{\partial\bar{v}}{\partial z} \qquad (3)$$

Here, we assume that shear production is dominant, and convective motions are negligible. Simpson et al. (2005) demonstrated that buoyancy production due to overstraining is typically below 10% of turbulent energy production, and a much smaller contributor to tidally-integrated production.

The eddy viscosity (A_z) is also directly available from the ADCP measurements (Lu and Lueck, 1999):

$$A_z = \frac{1}{\rho} \frac{P}{\left(\partial \bar{u}/\partial z\right)^2 + \left(\partial \bar{v}/\partial z\right)^2} \quad (4)$$

2.2 ADCP turbulence quality control

Quality control for eight million vertical profiles of velocity, and resulting measurements of turbulence parameters, requires objective, automated methods for correcting or masking biased data. We blank out turbulence data in regions with frequent occurrence of negative TKE production (Rippeth et al., 2003), likely indicating low turbulence levels or very small turbulent length scales. Surface waves can lead to a bias in τ due to the presence of strong non-turbulent water motions (Rippeth et al., 2003), and researchers often manually detect wave bias by looking for cases where stress increases up to the sea surface. We have developed a conservative technique where the coherence between a given beam's sea surface height (h_i; measurement discussed below) and its raw along-beam velocity (b_i) is used to identify depths and periods with potential for wave bias. This is particularly useful because it is an objective technique and depends only on ADCP measurements. If the coherence between h_i and b_i at any frequency is 0.1 or above, we blank out that data cell and all above it. Using this technique, we omitted data at depths greater than 4 m 21% of the time, and greater than 10 m 2.5% of the time.

A comparison of low and high-resolution datasets is typically used to estimate the low-bias in stress due to averaging in time and space, resolution bias (Lu et al., 2000; Rippeth et al., 2002). We estimate resolution bias by averaging neighboring beam velocity data in pairs (temporally or vertically) to create a new dataset with half the sample density (the "low resolution" dataset), and compare the resulting Reynolds stress estimates in linear regressions against those obtained with the full data set (the "high resolution" dataset). Using this approach, we estimate that stress is

underestimated on average by 23% due to resolution bias, and scale our stress observations up by this percentage.

2.3 Acoustic backscatter observations of turbulent structures and sea-surface height

An important component of our ADCP dataset is the acoustic backscatter (ABS), which has successfully been used in estuaries to observe coherent turbulent structures (e.g. Geyer and Smith, 1987; Seim and Gregg, 1994). Acoustic backscatter data were corrected for range-dependent spreading and attenuation (Deines, 1999).

We also use raw ADCP acoustic backscatter (ABS) data from each beam separately to obtain a time series of sea surface height, h_i (Visbeck and Fischer, 1995). This method has much higher resolution than the vertical cell height, because a parabolic fit of ABS is used to more precisely estimate h_i. ABS was linearly de-trended prior to surface height detection to account for possible strong ABS from suspended sediment. This approach is useful for surface wave detection, though our mode-12 subsample averaging smooths h_i over ~0.6 second periods, causing underestimation of the height of high-frequency waves. One must have at least two samples per wave period for detection, so the maximum frequency wave we can detect is 0.25 Hz.

3. Analyses

Computations using the data described above include turbulence parameters, boundary layer heights, and cross-correlation analyses that relate an integral measure of turbulence to external variables. Bed stress, τ_b, was computed using linear regressions toward the bed of the bottom five

stress measurements in the water column (at heights of 1.75 - 3.25 m). ADCP measurements of the mean squared shear (Geyer and Smith, 1987) were computed using 30-second velocity averages:

$$S^2 = \overline{(\partial u/\partial z)^2 + (\partial v/\partial z)^2} \quad (5)$$

Estimates of the local buoyancy frequency were computed using the CTD transect data:

$$N = [(g/\rho)(\partial\rho/\partial z)]^{0.5} \quad (6)$$

The full water column "bulk" buoyancy frequency was computed similarly, using only the surface and bottom density estimates near the ADCP sites. Mean squared shear was averaged over the full water column and combined with bulk buoyancy to compute the bulk gradient Richardson number:

$$Ri_{bulk} = N^2/S^2 \quad (7)$$

The Richardson number is useful for diagnosing the dynamic stability of the water column, with values below 0.25 typically indicating potential for instability (Geyer and Smith, 1987).

3.1 Layer definitions

Basic features of the turbulence observations motivate a quantitative separation into bottom boundary layer (BBL) and internal mixing layer (IML) turbulence. Regressions of shear velocity ($U_* = (\tau_b/\rho)^{0.5}$) cubed should correlate well against depth-integrated shear production when turbulence is strong, if bed friction is the dominant mechanism for turbulence generation (Lewis, 1996; Peters and Bokhorst, 2000). At Site B, a moderate correlation is observed, with 52% of the variance in vertically integrated P being explained by U_*^3 (**Fig. 4**). This correlation would likely be higher if we had more reliable estimates of τ_b; our method relies on extrapolation toward the bed. Nevertheless, at Site C, there are clearly two regimes -- one where turbulence is strong yet U_* is small, and another where the two variables correlate more strongly.

The general concept of separating IML and BBL turbulence was presented by Dyer (1997, p.53), wherein the IML and BBL can overlap (**Fig. 1**). We loosely follow that model and define IML turbulence as that which is detected above the top of the logarithmic velocity layer. This definition quantifies turbulence that is not a direct result of frictional forcing from the bed. The height of the logarithmic velocity layer (δ_{log}) was computed following methods given in Lu and Lueck (1997), and is the highest level to which there is a regression with no more than 1% discrepancy between observed and best-fit velocity. The minimum possible successful fit gives δ_{log} = 2.75 m, using the first three ADCP velocity bins for a 3-point linear regression. This is likely to be an outer log layer, not related to skin friction, and we typically do not observe a constant turbulent stress in the layer. The tidal maximum δ_{log} was typically about half the total water column depth during spring tides. Waves typically accompanied strong wind stress events, so no direct wind generated turbulence was detected without being masked to avoid wave bias in τ_z (**Sec. 2.2**).

We define the bottom boundary layer (BBL) as the continuously turbulent range of heights above the bed, capped by either (a) a zero intercept (stress) in a regression of near-bed stress versus height, or (b) the height where turbulent stress is not detected (where there are two successive omitted turbulent stress measurements in the quality-control procedures summarized in **Sec. 2.2**). In case (a), the top of the bottom boundary layer (δ_{BBL}) is identified using linear extrapolation of the lower water column (z <= 3.8m; 5 data points) stress profile upward to find a z-intercept. The 20-minute average turbulent stress profiles typically are linear through most of the BBL. However, only regressions with r^2>0.7 are used for estimating δ_{BBL}, and otherwise, the most recent height estimate is maintained. Resulting values for δ_{log} and δ_{BBL} were de-spiked with a 5-point median filter (25 minutes) and are presented and discussed in **Sec. 4**.

3.2 Cross-correlation analyses

A cross-correlation analysis enables us to examine how IML and BBL turbulence at each site responds to external forcing such as tidal range, wind, and freshwater input at Green Island (**Table 1**). Production (P) is a useful integral measure of turbulence, and when tidally averaged, is directly proportional to energy dissipation and buoyancy flux (Rippeth et al., 2003). The integrated production ($P_{int,}$) in the bottom boundary layer and internal mixing layer were computed by integrating P over these layers and over successive 24.84-hour periods (one tidal day), though this was limited to the depths where we have measurements (**Fig. 3g,h**).

"Driver variables" in the correlation analysis include external forcing parameters riverflow (squared, Q^2), east-west and north-south wind velocity (cubed, $U_{wind,1}{}^3$ and $U_{wind,2}{}^3$), and semidiurnal tidal range (cubed, $D2^3$). Additionally, the bulk buoyancy frequency squared (N^2) was utilized as a driver variable, to examine the role of local stratification effects. The powers for the driver variables were chosen to represent expected physical behavior, considering for instance that P_{int} (or dissipation) should be proportional to velocity cubed and velocity should be proportional to wave height. These powers also generally showed the most significant correlations, when contrasted against correlation analysis results using other powers.

We estimate significance for the correlations using a bootstrap technique that accounts for temporal autocovariance in driver variables (Martinson and Ianuzzi, 2003). Synthetic time series are created with identical mean, variance and power spectra as the driver variable. The driver variable's power spectrum is inverted with random phase, to create a synthetic "colored noise" time series, which is then cross-correlated against P_{int}. The result of 1000 repetitions is an empirical PDF of maximum (across all lags) absolute value correlation coefficients, from which

we can see the number of times our regression coefficient was exceeded by random chance. Taking the maximum over all lags conservatively assigns significance, but is appropriate because we are presenting maximum coefficients over all lags for our results table. The maximum lag in the cross-correlation analysis was chosen to be 8 tidal days, long enough to capture neap-spring tidal period relationships. Results are presented in **Sec. 4**, and discussed in **Sec. 5.3**.

4. Results

Along-channel CTD transects show that stratification generally increases with decreasing semi-diurnal tidal range (**Fig. 5**). High riverflow increases stratification in saline regions of the estuary, and dramatically enhances the neap-spring variability in stratification (**Fig. 6**). The 2004 transects and bottom water density time series (e.g. **Fig. 3d**) show patterns that are consistent with this stratification climatology. Both sites exhibited large neap-spring variations in stratification, and salinity was lower at Site C due to its location near the head of the salt intrusion.

We present ADCP data in three forms: (1) close ups of neap-to-spring transitions for the two sites during a period of high riverflow (**Fig. 7**), (2) 20-minute zoom-ins from within that figure to episodes of vigorous IML/BBL turbulence (**Fig. 8a**) and IML turbulence (**Fig. 8b**), and (3) profile averages for these zoom-in periods (**Fig. 9**). Site B shows abrupt changes in the turbulence and velocity fields at day 95 due to the onset of a wind event (west-northwesterly winds at 10-15 m s^{-1}), although the change in stratification appears to be gradual (**Fig. 7a**). Turbulence is stronger on flood tide while there is stratification, then on ebb tide after the stratification is eliminated. At Site C, there appear to be two different patterns of velocity and turbulence (**Fig. 7b**). Prior to the breakdown of stratification, velocity does not ebb at all near the bed, and shear is strong

throughout the water column (**Fig. 9b**). Turbulent stress magnitude maxima occur at mid-depth during ebb tides, and there are few signs of a turbulent bottom boundary layer. Approaching spring tide, which occurred on day 97, velocity becomes more uniform through depth. The largest turbulent stress is near the bed but turbulence occurs throughout the water column.

Strong episodes of IML turbulence are well-characterized by acoustic backscatter, with patterns resembling piled up billows (Seim and Gregg, 1994), breaking internal waves, waves distorted by shear, and widespread Kelvin-Helmholtz instabilities (Strang and Fernando, 2001). At Site C, IML turbulence was strongest during stratified ebb tides, at the time when ebb currents were maximal and shear strong throughout the water column (**Fig. 8**). Characteristic turbulent (Ellison) length scales are typically larger than the 0.5 m ADCP resolution (**Fig. 9**), and ABS clearly identifies coherent turbulent structures. At Site B, IML turbulence is strongest at peak flood, but is also moderate in association with a 1-3 m thick shear layer (0.15-0.25 s^{-1}) that persists into slack tide. Length scales at Site B are similar to or larger than the ADCP resolution, and coherent events (likely sediment resuspension) are visible in ABS in the lower water column.

Cross-correlation results are shown in **Table 1**, and discussed in detail in **Sec. 5.3**. Here, we focus on correlations significant at the >90% level only, shaded in the table. Tidal range correlations are often highly significant, riverflow correlations are only significant for Site C, wind correlations are only significant in one case, and bulk buoyancy frequency correlations are very strong. Specifically, the correlation between Site B BBL P_{int} and D2 range is positive and significant at 1 tidal day lag ($\alpha = 0.001$), and for Site C BBL P_{int} an D2 range it is also highly significant at a 2 day lag ($\alpha = 0.001$). The correlation between Site B IML P_{int} and D2 range is significant at a 0 day lag ($\alpha=0.02$). The negative correlation between Site C IML P_{int} and D2 range is significant, with

the largest correlation ($\alpha = 0.06$) when P_{int} minima trails D2 range maxima by 2 or 3 tidal days (i.e. trails spring tide). The positive correlation between Site C BBL P_{int} and Q is significant ($\alpha = 0.08$) with P_{int} trailing Q by 8 days, while the correlation between Site C IML P_{int} and Q is significant at a 0-1 day lag ($\alpha = 0.06$). Correlation results for P_{int} with wind were only significant for Site C IML P_{int} ($\alpha=0.04$), which would indicate that turbulence is strong three days before a period with a strong east wind. Significant negative correlations exist for Site B and C BBL P_{int} with bulk N^2 ($\alpha=0.03$ and $\alpha=0.02$), and a highly significant positive correlation exists for Site C IML P_{int} with bulk N^2 ($\alpha<0.001$). The relationship between N and IML turbulence is further demonstrated in **Fig. 10**.

5. Discussion

To our knowledge, ours is the first study to contrast the intensity and variability of observed estuarine IML and BBL turbulence over a broad range of forcing. Furthermore, the sites provide a sharp contrast; Site B is more representative of channelized "rectangular" estuary dynamics, while Site C is a region with changing channel depth and width near the head of the salt intrusion. At Site C, the proportion of turbulence occurring in the IML is often near 100%, with no log layer. At Site B, the proportion typically varies from 30-60% (**Fig. 10**). A prior study evaluating the relative magnitude of observed log layer and IML turbulence between George Washington Bridge and The Battery also found that IML turbulence was strong, but also found that the depth-averaged dissipation was generally well-predicted as bed-driven (logarithmic layer) shear production (Peters and Bokhorst, 2000).

Some limitations to the scope of our study are worth mentioning. Our ability to quantify turbulence close to the sea surface, seafloor and in weakly turbulent stratified regions (e.g. the pycnocline in certain cases) is limited due to the half-meter vertical averaging length and the fact that the ADCP cannot collect data at the upper and lower edges of the water column. The majority of shear production and dissipation is expected to occur below 1.75 m when turbulence is bottom-driven (Peters and Bokhorst, 2000), so our observations of BBL P_{int} may be underestimates, if one is interested in flow energetics. Finer-scale measurements will be useful to shed further light on turbulence in these regions, and we recommend short microstructure surveys alongside long-term ADCP measurements.

This is also the first published account where the ADCP variance method was used to study IML turbulence, and the first study of (at times) strongly stratified conditions (local $N>0.1\ s^{-1}$), so we cannot take for granted that the turbulence observations are not biased by internal waves during these periods. Below, we address this concern and briefly examine the mechanisms driving shear and turbulence at both sites. We then contrast variability in IML and BBL turbulence on timescales of days to seasons, the main focus of this paper. We conclude **Sec. 5** by discussing the implications for estuarine transports, residence times and air-water gas transfer.

5.1. Forcing of Site C IML turbulence

Site C exhibits unusual IML turbulence patterns never before observed at this level of detail in the Hudson, yet they are robust and physically sensible considering local bathymetry and observed currents. The patterns fit more closely to the isolated turbulence layers concept of **Fig. 1b**, though in many cases the BBL is non-existent or confined very close to the bed. Bottom friction is clearly not driving turbulence during and after neap tide, as P is highest during ebb tide when near-bed

currents are near zero (**Fig. 7b**). Strong ebb currents flow over the slowly flooding near-bed layer, exhibiting strong shear. This occurs because there is a ~1% downward slope toward the north and a sharp slope to isopycnals at neap and post-neap transitional tides (**Fig. 5**) that leads to an up-estuary baroclinic pressure force near the bed. Stenstrom (2004) used a numerical model in non-hydrostatic mode (on a coarse grid; not a large eddy simulation) to examine the role of bed slope and channel width in the Hudson. He concluded that turbulent mixing was highly dependent upon local bed slope.

ADCP stress observations from a period such as that shown in **Fig. 8b** should be reliable because the assumptions of the variance method (**Sec. 2.1**) are likely to be valid. One assumption is for horizontal homogeneity – the first statistical moments (e.g. $\bar{u}$) of the flow must be uniform across the ADCP beam spread in order to accurately observe the mean velocity, and the second statistical moments of the flow (e.g. $\overline{u'^2}, \overline{u'w'}$) must be uniform across the beam spread to observe the turbulent stress with the variance method. Lu and Lueck (1999) suggested a simple test of the former assumption: The averaging time should greatly exceed L/U, the distance between beams divided by the mean velocity. At mid-depth, the beam spread is about 5 m, the mean along-stream velocity is 0.5 m s^{-1}, and the ratio L/U equals 10 s, over two orders of magnitude lower than the averaging time of 20 minutes; thus, the assumption is reasonable for first moments. The second moments, when computed over 20-minute periods, should generally not vary over dramatically smaller distances than the first moments, so the second assumption is also likely valid.

The vertical excursions of acoustic backscatter (ABS) and strong aperiodic vertical velocities in **Fig. 8b** support our contention that the high stress and P measurements reflect true vertical momentum and mass fluxes. ABS shows angled features that start high in the water column and

migrate down in the water column over periods of about one minute. In an estuary, a common interpretation for peaks in ABS (away from the bed) is that they identify regions of turbulent salinity microstructure (Seim, 1999). We interpret these ABS maxima as regions with small-scale turbulence at the edges of large-scale turbulent billows that are piling upon one another and being deformed due to the strong shear. The downward phase propagation of the features is due to the upper part a given billow (10 m height) being moved much more rapidly downstream than the lower part (5 m height).

The bulk Richardson number is somewhat useful for understanding the forcing of turbulence at this site, when combined with clues from the CTD database. The period shown in **Fig. 8b** exhibits a Ri_{bulk} of 0.23. Shear is spread through the water column, whereas CTD profiles at this site from periods with similar conditions show that the vertical density gradient occurs over a much smaller range of depths, in a pycnocline. The *local* Richardson number in the pycnocline should be higher than the *bulk* Richardson number for such a period. Therefore, it is likely that the local gradient Richardson number at the pycnocline for **Fig. 8b** was above 0.25, and mixing was a one-way upward entrainment process, not a two-way diffusion process – a particular challenge for numerical models (Sharples, 2005). Moreover, during the hour leading up to this highlighted period, Ri_{bulk} was from 0.25 to 0.75, and the local Richardson number in the pycnocline was likely higher. There were isolated yet periodic turbulent events evident in ABS, w, and turbulent stress during this period.

There is a minimum in channel width just north of Site C, where Stony Point cuts into the channel (**Fig. 2;** Nitsche et al., 2007), which could trigger internal hydraulic effects impacting Site C during stratified ebb tides. A lateral constriction can spawn trains of turbulent billows or internal

waves (e.g. Geyer and Smith, 1987; Seim and Gregg, 1994), possibly explaining some of our observations described above. The importance of lateral constrictions for turbulence in the Hudson has been examined around the channel constriction at George Washington Bridge (Chant and Wilson, 2000; Peters, 2003; Stenstrom, 2004). Our long-term observations at Site C broaden our understanding of the impact of riverflow and tidal range on IML turbulence in a region with rapidly changing bathymetry (**Sec. 5.3**).

5.2. Forcing of Site B IML turbulence

Site B turbulence patterns fit more closely to the overlapping turbulence layers concept of **Fig. 1a**. The periods of strongest IML turbulence are during flood tides, when there is a local stress maximum between the bed and the mid-depth region of maximum shear (**Fig. 8a**). The bulk Richardson number is not useful during stratified Site B flood tides, as it is above 0.25 even when BBL or IML turbulence is strong, and thus is not a good local measure of stability. Near the bed, vigorously turbulent velocities and pulses of high acoustic backscatter suggest that the local Richardson number is below 0.25 and shear instability is the turbulence generation mechanism.

Brief periods of strong turbulence are also often observed as vigorously turbulent front-like features pass the ADCP with very high near-surface acoustic backscatter, a common observation when ADCP measurements are made around sea-surface fronts (Marmorino and Trump, 1996). A front at year-day 94.07 provided ~15% of the flood tide's IML TKE production, though turbulence was only elevated for about 10 minutes. Similarly, turbulence within 100 m behind a propagating river plume front was estimated to provide 20% of the total plume mixing (Orton and Jay, 2005).

A surprising result is the moderate shear production at Site B high in the water column during the slack after flood (e.g. day 94.13). One prior study of "direct" ADCP measurements of turbulent stress ($\rho\overline{u'w'}$, not utilizing the variance method) at the same semi-diurnal tidal phase in a more weakly stratified estuarine pycnocline found qualitative agreement with a small number of microstructure turbulence profiles (Ott et al., 2002). In our data, these periods are responsible only for a small fraction of total IML turbulence (P_{int}), but warrant further analysis. The computed characteristic vertical length scale (Ellison) is ~0.5 m, yet the integral horizontal length scale (L_H) for stress (Stacey et al., 1999a) increases with height from ~2 m near the bed to ~50 m near the shear layer. This may reflect production of turbulence at the scales of internal gravity waves (e.g. sheared wave breaking), but may also reflect stress biases related to internal wave motions. A further possibility is convective motions, which have been shown to account for more than 10% of turbulent kinetic energy production at the end of flood tide in a partially mixed estuary (Simpson et al., 2005). To verify that internal waves were not biasing the results of our study, we separately computed stress in 15-second periods (with averaging afterward), excluding contributions to stress from longer-period motions. This conservatively excludes motions directly associated with internal waves, which have a maximum frequency of N – our CTD database shows N is always below 0.2 s^{-1} (2 cycles per minute) at the ADCP sites (**Fig. 6**). Results of the new correlation analyses are highly similar to those displayed in **Table 1**. Nevertheless, these results underline the need for additional verification of ADCP stress measurements at the pycnocline in stratified shear flows.

5.3. IML and BBL turbulence variability on sub-tidal to seasonal timescales

The cross-correlation analysis summarized in **Table 1** and **Secs. 3.2 and 4** is useful for seeking external forcing agents that cause variability in Hudson IML and BBL turbulence. Results are

generally consistent with strong tidal control (14 day period) of both BBL and IML turbulence, related to neap-spring variations in stratification. They are also consistent with riverflow exerting influence on both types of turbulence at Site C, with the interesting result that IML turbulence at that site increases during periods of high river flow. However, as with any correlation analysis, one cannot distinguish significant correlations arising from physical connections from those that can be expected to arise from noise. Here, we examine the most significant correlations and seek consistent physical explanations.

Cross-correlation results suggest that fortnightly modulation of the semi-diurnal tidal range has a very strong effect on BBL and IML turbulence, though with varying phase. The highly significant positive correlations between BBL P_{int} and D2 tidal range at both sites are not surprising, as tides are generally understood to be the main drivers of BBL turbulence in partially mixed estuaries (Peters, 1999; Geyer et al., 2000). Turbulence in an estuarine BBL is produced due to interaction of tidal currents with the frictional bottom boundary, and because these current velocities increase with increasing tidal range, so does the intensity of the turbulence (to first order). D2 tidal range is inversely correlated with IML turbulence at Site C, with a two day lag (on average, P_{int} minima occurs 3 days after spring tide, during a post-spring transitional tide).

The phase lags of the significant Site C correlations between turbulence and tidal range represent a hysteresis pattern between turbulence in either layer and the fortnightly tidal phase, as shown in **Fig. 11**. The pattern was strong in the first half of the study period, and moderate in the latter half. This pattern likely exists due to a similar hysteresis that occurs between D2 range and stratification (N^2) in the Hudson (Bowen and Geyer, 2003). Hysteresis between stratification and tidal range is a fundamental feature in moderate depth (~20 m) partially mixed estuaries

(MacCready, 1999). The stratification hysteresis was also stronger in the first half of the study, likely due to weaker neap tides or unsteadiness of the estuarine circulation and salt intrusion in the face of rapidly changing riverflow and tidal forcing. For cycle #1 (**Fig. 11**), during the post-spring transitional tide, bulk N^2 was 25 times smaller than during the post-neap transition, for the same tidal range. During cycle #5, the difference in N^2 was only a factor of 4. The turbulence hysteresis likely follows the intensity of the stratification hysteresis, considering the strong in-phase correlations of N^2 with IML or BBL turbulence.

A likely mechanism for increased stratification (and decreased tidal range) increasing IML turbulence is increased shear due to increased baroclinic forcing. The strongest Site C IML turbulence for the first neap-spring cycle occurred from 2-5 days after neap, because neap tide up-estuary salt pumping built stratification to maximal levels, and mean vertical shear was as high as 0.14 s^{-1} (in contrast, the mean shear during spring tides is 0.04 s^{-1}).

Prior studies have observed impacts of strong winds in the Hudson, either through the indirect effect of sea-surface height forcing due to Ekman transport in the New York Bight (Peters and Bokhorst, 2000), or the more direct effect of wind shearing the upper water column (Peters, 1999). Due to conservative removal of turbulence data with potential for wave bias (see **Sec. 2.2**), the only influence of wind on turbulence we may see in our data is through straining the density field or coastal sea level set-up. Our correlation analysis of wind and integrated TKE production (P_{int}), however, did not support the hypothesis of a substantial causal relationship. The one significant wind correlation is consistent with IML turbulence being strong three days before a period with a strong east wind, which does not appear to have any physical explanation. This result was strongly dependent on only one wind event that occurred during high riverflow soon after neap tide, so can

be explained with other significantly correlated variables. Moreover, three other east-west wind events had no sign of elevated turbulence.

The spring season typically has higher riverflow (Q) into the estuary than any other season (USGS, 2006), with impacts on stratification and turbulence. Higher riverflow is associated with enhanced stratification, with the exception being cases where high riverflow spring tides flush all stratification seaward of a given site. The summer season has the lowest riverflow, with the exception being rare storms. Positive correlations when BBL P_{int} lags 8 days behind Q at Sites B and C are marginally significant ($\alpha = 0.12$ and $\alpha = 0.08$, respectively). These correlations and the substantial lag may arise from the tendency for sustained high riverflow events (e.g. the freshet) to wash the salt wedge seaward of the site, reducing stratification to riverine levels and allowing stronger turbulence.

The impact of increasing riverflow on IML turbulence at Site C is unique, and likely related to local bathymetry, discussed in **Sec. 5.1**. The positive correlation between Site C IML P_{int} and riverflow is significant at a 0 or 1 day lag (α=0.06 for both lags). This lag is reasonable, considering that approximating the travel time for changes in river stage from Green Island to the study area as shallow water wave propagation, $c = \sqrt{gh}$, gives a travel time of six hours.

The mechanism for increased river flow increasing IML turbulence at Site C is not clear because it should increase barotropic forcing, not baroclinic forcing, so have little effect on shear. Possible mechanisms are: (1) Shear can be set up by differential friction on the bottom layer, with an effect much like that of a baroclinic pressure gradient force (Monismith and Fong, 1996). (2) Increased internal hydraulic effects, which can cause IML turbulence regardless of the local Richardson

number. An increased barotropic pressure gradient likely drives stronger ebb currents in both the surface and bottom layers at Stony Point, increasing the two-layer composite internal Froude number, $G^2 = u_1^2/(g'h_1) + u_2^2/(g'h_2)$, where g' is reduced gravity $g(\rho_0 - \rho_1)/\rho$, u is velocity, h is layer thickness, and subscripts denote layer numbers (Armi, 1986). The Hudson is mostly confined to a channel by geologic features, and this result might not be observed in estuaries with a larger floodplain, where high riverflow may not necessarily increase ebb tide currents.

There was moderate correlation between Site C bulk N and riverflow during the study period (r^2 = 0.22). The cross-correlation analysis shows that stratification has a very strong influence on IML turbulence, so it is useful to look at how riverflow improves that correlation when added in a multiple linear regression. It is important to only consider cases where Site C has moderate stratification, which is required for all the mechanisms discussed above. Including cases of bulk N>0.05 s^{-1} only, a linear regression of IML P_{int} with N^2 gives an r^2 value of 0.46, whereas adding Q^2 in a multiple linear regression gives an improved r^2 of 0.61. That is, when at least mildly stratified, a linear model of IML P_{int} that includes stratification and riverflow performs substantially better than one including only stratification.

5.4 Implications for estuarine circulation, modeling and transports

Studies have clarified the important role of bottom boundary layer (BBL) turbulence for estuarine circulation (e.g. Geyer et al., 2000; Chant et al., 2007), but few observational studies exist quantifying IML turbulence and its role. Here, we have shown that IML turbulence, represented by TKE production, is maximal when the BBL turbulence in the estuary is at a minimum (**Figs. 3, 10, 11**) – during a neap or post-neap transitional tide, and (for Site C) stratified periods with high river input. The observed intensity and temporal variability for IML turbulence also has important

implications for scalar transports, because vertical fluxes of buoyancy and dissolved constituents in stratified waters are approximately proportional to P (Rippeth, 2005). Moreover, these observations suggest that the mixing efficiency may be at its highest during neap and post-neap transitional tides, because IML turbulence acts near the pycnocline, whereas BBL turbulence predominantly stirs well-mixed water. Extrapolating our results to estuary-wide budgets will require observations with greater spatial coverage, but below we discuss several important implications of these observations for energetics and circulation modeling, then for scalar transports.

This increased importance of IML turbulence during neap and post-neap transitional tides provides an important test for estuarine models. These are the periods that have provided the greatest discrepancy between observed and modeled estuarine circulation from an analytical (Geyer et al., 2000) and a numerical model (Warner et al., 2005). Our observations show that strong IML turbulence increases the drag on the upper layer flow during such periods, which should reduce the magnitude of the estuarine exchange velocity. Models developed with the assumption that all turbulence is related to bed friction, or having mixing parameterizations that require manual adjustments for background turbulence, will generally have difficulty modeling circulation during neap and post-neap transitional tides. Modifying mixing parameterizations to better account for IML turbulence may improve model predictions.

Examining the Hudson's energy budget, Peters (2003) concluded from microstructure turbulence measurements that the localized region of elevated IML dissipation near the George Washington Bridge (GWB) did not appear to be of great importance. However, that study acknowledged that only a narrow range of conditions were sampled. Our results show tidally-averaged pycnocline

TKE production rates at Site C that are as much as a factor of 10 higher than dissipation rates in that study, and suggest that the estuary-wide importance of IML turbulence at GWB should be re-evaluated for both high riverflow conditions and periods of peak stratification.

Our results have particularly strong implications for estuarine trapping of river-derived sediment and particle-associated pollutants during flood events such as the spring freshet. The buoyant fresh water and associated stratification that arrives with these constituents can weaken vertical mixing, yet our results suggest that IML turbulence in bathymetrically complex regions is increased during these periods. Fine suspended sediment transport should be highly sensitive to IML turbulence due to entrainment of saltwater into the upper layer and the non-linearity of flocculation. Flocculation is the aggregation of riverine particles when exposed to saline water, increasing settling rates by a factor of 10-100 (Kineke and Sternberg, 1989), typically with a threshold onset at salinities of 1-2 (Dyer, 1986, p. 204). In our observations, the surface salinity (1 m depth) is never below 2 at George Washington Bridge or southward, with riverflow as high as 1800 $m^3 s^{-1}$. A significant fraction of river-derived fine sediments are therefore flocculating and settling to the bed, preventing or delaying export. Unsurprisingly, the Hudson appears to generally be depositional in the region south from GWB, except in rare ~10 year events where very high riverflow coincides with a spring tide (Geyer et al., 2002). A model that doesn't accurately predict IML turbulence under a wide range of stratification will be less likely to predict these sediment trapping patterns accurately.

IML turbulence can enhance air-water gas transfer, as it increases turbulent overturning near the sea surface. This is illustrated in **Fig. 7**, when Site C upper water column P is higher during post-neap transitional ebb tides than it is at Site B during vigorously mixed spring tides, with sustained

values of 10^{-1} W m^{-3}. P is roughly proportional to dissipation ε (Rippeth et al., 2003), and gas transfer typically goes as dissipation near the sea-surface (Zappa et al., 2007), so high IML P should enhance air-water gas transfer. The role may be especially important around sea-surface fronts (where the IML intersects with the sea-surface) which we found to cause 15% of P_{int} at Site B, and also cause bubble injection (Marmorino and Trump, 1996). Moreover, many pollutants that are remobilized during floods and freshets (e.g. PCBs, N_2O, PAH) have a gaseous phase and thus their transport (and possible evasion from water to air) will be particularly affected by IML turbulence during these stratified periods.

6. Summary and Conclusions

We have used along-channel density transects and two continuous 100-day full water column turbulence datasets to characterize stratification and turbulence in the Hudson River estuary. Separately, we quantify bottom boundary layer (BBL) and internal mixing layer (IML) turbulence, the latter of which is increasingly being recognized for its importance for scalar transports in the coastal ocean (Rippeth, 2005). The ADCP sites are chosen to maximize dynamical contrast, and thus display a diverse range of turbulence processes; Site B is in channelized regular bathymetry, while Site C is in a region of more complex bathymetry, with depth increasing up-river. While extrapolating our results to estuary-wide budgets will require measurements at a wider range of along-channel locations, several important conclusions are reached.

Prior studies have suggested that BBL turbulence dominates in the Hudson, at least for estuarine dynamics (Geyer et al., 2000; Chant et al., 2007), and our results for Site B generally do not contradict those. However, we observe relatively strong IML turbulence that doesn't fit that model

during neap or post-neap transitional tides (between neap and spring), and that is particularly strong and independent of bed-stress at Site C. This expands upon the findings of Stenstrom (2004), who showed with a non-hydrostatic numerical model of the Hudson that IML mixing is spatially variable, with turbulent mixing during stratified periods highly dependent upon local bed slope.

A major advantage of ADCP turbulence measurements is that our long-term autonomous deployments also capture the role of unpredictable extremes in riverflow and wind, as well as extreme tides. While bottom boundary layer turbulence is generally dominant at spring and post-spring transitional tides in the estuary, we find an increasing relative magnitude for IML turbulence at times of maximum stratification (at neap or the post-neap transition) and riverflow. Duplication of these differing patterns of BBL and IML turbulence provides a stringent test for numerical models, but an important one if they are to accurately predict transports of constituents through partially mixed or highly stratified estuaries.

Acknowledgements

The authors would like to thank John Lipscomb, captain for the Hudson Riverkeeper, for conducting the along-channel CTD surveys; Bruce Huber and Frank Nitsche for field and mapping assistance; Wade McGillis, Bob Houghton and Arnold Gordon for funding and guidance; and Rocky Geyer (WHOI) for discerning comments. Research was funded by the NSF project, "Collaborative Research, Determining the Air-Water CO2 Flux in Coastal Systems" (grant #0526677), the Environmental Protection Agency's Science to Achieve Results (STAR) Program

(grant R830976), and by a graduate fellowship in the Department of Earth and Environmental Sciences at Columbia University.

References

Armi, L., 1986. The Hydraulics of two flowing layers with different densities. Journal of Fluid Mechanics 163, 27-58.

Bowen, M. M., and W. Rockwell Geyer, Salt transport and the time-dependent salt balance of a partially stratified estuary, J. Geophys. Res., 108(C5), 3158, doi:10.1029/2001JC001231, 2003.

Chant, R.J., Geyer, W.R., Houghton, R., Hunter, E., Lerczak, J., 2007. Estuarine boundary layer mixing processes: Insights from dye experiments. In press, Journal of Physical Oceanography.

Chant, R. J., Wilson, R.E., 2000. Internal hydraulics and mixing in a highly stratified estuary. Journal of Geophysical Research 105, 14,215-14,222.

Deines, K. L., 1999. BBADCP- Backscatter estimation using broadband acoustic Doppler current pro-filers. In: Anderson, S. P., Terray, E.A., Rizzoli White, J. A., Williams, A. J. III (Eds.), Proceedings of the IEEE Sixth Working Conference on Current Measurement, pp. 258-263.

Dyer, K.R., 1986. Coastal and Estuarine Sediment Dynamics. Wiley-Interscience, New York.

Dyer, K.R., 1997. Estuaries, a Physical Introduction, 2nd Edition. John Wiley & Sons, New York.

Flinchem, E. P., Jay, D.A., 2000. An introduction to wavelet transform tidal analysis methods. Estuarine, Coastal and Shelf Science 51, 177–200.

Gargett, A., Wells, J., Tejada-Martinez, E., Grosch, C. E., 2004. Langmuir supercells: A mechanism for sediment resuspension and transport in shallow seas. Science 306, 1925-1928.

Geyer, W.R., Smith, J.D., 1987. Shear instability in a highly stratified estuary. Journal of Physical Oceanography 17, 1668-1679.

Geyer, W. R., Trowbridge, J.H., Bowen, M.M., 2000. The dynamics of a partially mixed estuary. Journal of Physical Oceanography 30, 2035-2048.

Kineke, G. C. and Sternberg, R.W., 1989. The effect of particle settling velocity on computer suspended sediment concentration profiles. Marine Geology 90, 159-174.

Large, W. G., Pond, S., 1981. Open ocean momentum flux measurements in moderate to strong winds. Journal of Physical Oceanography 11, 324– 336.

Lewis, R.E., 1996. Relative contributions of interfacial and bed generated mixing to the estuarine energy balance. In: Pattiaratchi, C. (Ed.), Mixing in Estuaries and Coastal Seas, Coastal and Estuarine Studies Vol. 50. American Geophysical Union, Washington, D.C., p. 250-266.

Lu, Y., Lueck, R.G., 1997. The logarithmic layer in a tidal channel. Continental Shelf Research 17(14), 1785-1801.

Lu, Y., Lueck, R.G., 1999. Using a broadband ADCP in a tidal channel, part II: Turbulence. Journal of Atmospheric and Oceanic Technology 16, 1568-1579.

Lu, Y., Lueck, R.G., Huang, D., 2000. Turbulence characteristics in a tidal channel. Journal of Physical Oceanography 30, 855–867.

MacCready P., 1999. Estuarine adjustment to changes in river flow and tidal mixing. Journal of Physical Oceanography 29, 708–726.

Marmorino, G.O., Trump, C.L., 1996. High resolution measurements made across a tidal intrusion front. Journal of Geophysical Research 101(C11), 25661-25674.

Martinson, D.G., Iannuzzi, R.A., 2003. Spatial/temporal patterns in Weddell gyre characteristics and their relationship to global climate..Journal of Geophysical Research 108, doi: 1029/2000JC000538.

Monismith, S.G., Fong, D.A., 1996. A simple model of mixing in stratified flows. Journal of Geophysical Research 101 (C12), 28583-28595.

Nitsche, F. O., Ryan, W.B.F., Carbotte, S. M., Bell, R. E., Slagle, A., Bertinado, C., Flood, R., Kenna, T., McHugh, C., 2006. Regional Patterns and Local Variations of Sediment Distribution in the Hudson River Estuary. Estuarine Coastal and Shelf Science 71, 259-277.

NOAA, 2006. National Oceanographic and Atmospheric Administration, National Data Buoy Center data available on the World Wide Web, accessed February 10, 2006, at URL http://ndbc.noaa.gov/

NOAA-NOS, 2006. National Oceanographic and Atmospheric Administration, National Ocean Service data available on the World Wide Web, accessed February 10, 2006, at URL http://spo.nos.noaa.gov/bathy/

Orton, P. M., Jay, D. A., 2005. Observations at the tidal plume front of a high-volume river outflow. Geophysical Research Letters 32, L11605, doi:10.1029/2005GL022372.

Ott, M.W., Dewey, R., Garrett, C., 2002. Reynolds stresses and secondary circulation in a stratified rotating shear flow. Journal of Physical Oceanography 32, 3249-3268.

Peters, H., 1999. Spatial and temporal variability of turbulent mixing in an estuary. Journal of Marine Research 57, 805-845.

Peters, H., 2003. Broadly distributed and locally enhanced turbulent mixing in a tidal estuary. Journal of Physical Oceanography 33, 1967-1977.

Peters, H., Bokhorst, R., 2000. Microstructure observations of turbulent mixing in a partially mixed estuary. I: Dissipation rates. Journal of Physical Oceanography 30, 1232-1244.

Peters, H., Johns, W.E., 2006. Bottom Layer Turbulence in the Red Sea Outflow Plume. Journal of Physical Oceanography36 (9), 1763–1785, DOI: 10.1175/JPO2939.1

Rippeth, T., 2005. Mixing in seasonally stratified shelf seas: a shifting paradigm. Philosophical Transactions of the Royal Society A 363, 2837-2854, (doi:10.1098/rsta.2005.1662).

Rippeth, T.P., Simpson, J.H. and Williams, E., 2003. Measurement of the rates of production and dissipation of turbulent kinetic energy in an energetic tidal flow: Red Wharf Bay revisited. Journal of Physical Oceanography 33, 1889-1901.

Rippeth, T.P., Williams, E., Simpson, J.H., 2002. Reynolds stress and Turbulent Kinetic Energy Production in a Tidal Channel. Journal of Physical Oceanography 32, 1242–1251.

Seim, H.E., 1999. Acoustic backscatter from salinity microstructure. Journal of Atmospheric and Oceanic Technology 16, 1491-1498.

Seim, H.E., Gregg, M.C., 1994. Detailed observations of a naturally occurring shear instability. Journal of Geophysical Research 99 (C5), 10049-10073.

Sharples, J., 2005. Turbulence measurements in highly stratified estuaries. In: Baumert, H., Simpson, J., Sundermann, J. (Eds.), Marine Turbulence, Theories, Observations and Models, Cambridge University Press.

Simpson, J. H., Crawford, W.R., Rippeth, T.P., Campbell, A.R., Cheok, J. V. S., 1996. The vertical structure of turbulent dissipation in shelf seas. Journal of Physical Oceanography 26, 1579-1590.

Simpson, J.H., Fisher, N.R., Wiles, P., 2004. Reynolds stress and TKE production in an estuary with a tidal bore. Estuarine, Coastal and Shelf Science 60, 619-627.

Simpson, J.H., Williams, E., Brasseur, L.H., Brubaker, J.M., 2005. The impact of tidal straining on the cycle of turbulence in a partially stratified estuary. Continental Shelf Research 25, 51-64.

Stacey, M.T., Monismith, S.G., Burau, J.R., 1999a. Measurements of Reynolds stress profiles in unstratified tidal flow. Journal of Geophysical Research 104, 10933-10949.

Stacey M. T., Monismith, S. G., Burau, 1999b. Observations of turbulence in a partially stratified estuary. Journal of Physical Oceanography 29, 1950–1970.

Stenstrom, P., 2004. Hydraulics and mixing in the Hudson River estuary: A numerical model study of tidal variations during neap tide conditions. Journal of Geophysical Research 109, C04019, doi:10.1029/2003JC001954.

Strang E.J., Fernando H.J.S.,. 2001. Entrainment and mixing in stratified shear flows. Journal of Fluid Mechanics 428, 349-86.

USGS, 2006. United States Geological Survey National Water Information System (NWISWeb) data available on the World Wide Web, accessed February 10, 2006, at URL http://waterdata.usgs.gov/nwis/.

Visbeck M., Fischer, J., 1995. Sea surface conditions remotely sensed by upward-looking ADCPs. Journal of Atmospheric and Oceanic Technology 12, 141–149.

Warner, J. C., Geyer, W. R., Lerczak, J. A., 2005. Numerical modeling of an estuary: A comprehensive skill assessment. Journal of Geophysical Research 110, C05001, doi:10.1029/2004JC002691.

Williams, E., Simpson, J.H., 2004. Uncertainties in estimates of Reynolds stress and TKE production rate using the ADCP variance method. Journal of Atmospheric and Oceanic Technology 21, 347-357.

Zappa, C.J., McGillis, W.R., Raymond, P.A., Edson, J.B., Hintsa, E.J., Zemmelink, H.J., Dacey, J.W.H., Ho, D.T., 2007. Environmental turbulent mixing controls on air-water gas exchange in marine and aquatic systems. Geophysical Research Letters 34, L10601, doi: 10.1029/2006GL028790.

Figure Captions

Fig. 1: Conceptual mixing layer diagram with salinity profiles and boundary layer heights (δ). Shown are examples of (a) the case where IML and BBL mixing interact, common in partially mixed estuaries, and (b) the case where the two layers are separate, common in highly stratified estuaries. Adapted from Dyer (1997, p.53).

Fig. 2: Hudson River estuary coastline (left) with a zoom-in (right panel) to shaded NOAA-NOS (2006) bathymetry data, and ADCP sites marked '+'. Along-channel distance up-estuary from The Battery (rkm 0 line) is also shown in river kilometers (rkm).

Fig. 3: Time series view of ambient conditions and turbulence variables during the ADCP deployments. Panel (a) shows freshwater input. Panels (b, c and d) show data derived from CTD observations at Site B (0.5 m above the bed), including total depth, semidiurnal (D2) and diurnal (D1) tidal ranges computed with a wavelet transform tidal analysis of depth, water density (σ_t). Panels (e) and (f) show estimates of bed stress (τ_b; **Sec. 3**) at Site B, and wind stress (τ_w). Panels (g) and (h) show integrated turbulent kinetic energy production (P_{int}; **Sec. 3.2**) for the IML and BBL. The dotted vertical line shows the beginning of the year day range for **Fig. 7**.

Fig. 4: Relationship between bed frictional forcing (U_*^3) and turbulence (vertically integrated shear production) for Sites B and C. For Site C, there appear to be two distinct regimes, one where turbulence increases with U_*^3, and another where it is strong in spite of low U_*^3.

Fig. 5: Three along-channel density transects during spring freshet season, for (a) a weak spring tide (2004 year-day 111, riverflow Q=470 $m^3\ s^{-1}$), (b) one day prior to neap tide (2004 year-day

117, Q=740 m^3 s^{-1}), and three days after neap tide (2005 year-day 108, Q=400 m^3 s^{-1}). Vertical red lines show the ADCP sites, and the thalweg depth is shaded black. The aspect ratio exaggerates bed topography, and actual bed slopes are rarely greater than one percent south of 41.2° N latitude. The salt intrusion length maximum typically lags behind the minimum in tidal forcing, with maximum intrusion length occurring during the post-neap transitional period (see **Sec. 5.3**).

Fig. 6: Summary of stratification (local N) observations the Hudson, with respect to along-channel location (latitude), riverflow (Q; prior 10-day mean) and semi-diurnal (D2; prior 5-day mean) tidal range. The plots summarize data from 30 along-channel transects like those in **Fig. 5**, between 2001 and 2006. Horizontal dotted lines show Sites B and C. Each colored box shows the observed maximum water column stratification from a single profile (from 1.5 m vertical running averages of density). Symbols are (WP) West Point, (IP) Indian Point, (TZ) Tappan Zee Bridge, (GW) George Washington Bridge, and (TB) The Battery.

Fig. 7: (a) Site B and (b) Site C zoom-ins of a neap-spring transition with high riverflow. Plotted variables are: density (σ_t), along-stream velocity (u), along-stream vertical shear ($\partial u/\partial z$), acoustic backscatter (ABS), turbulent stress (τ_{xz}), eddy viscosity (A_z), and turbulent kinetic energy production (P). Turbulence data is masked when it is likely dominated by noise (blanked white) or side lobe and wave contamination (grey; see **Sec. 2.2**). The sea surface and bottom boundary layer height (black lines), and log layer height (white line) are shown. The vertical dotted lines show the times for the two figures that follow. Site C exhibits no log layer within our measurement range for most of this period.

Fig. 8: Zoom-ins to 0.5 Hz raw data for 20-minute periods at (a) Site B, and (b) Site C. Shown are: along-stream velocity (u), vertical shear ($\partial u/\partial z$), vertical velocity (w), and acoustic backscatter from a single ADCP beam (ABS). For Site C, shear is box-filtered with a 1.5 m by 10 s window, due to excessive variability. The following plot shows averaged turbulent stress profiles from these periods.

Fig. 9: (a) Site B and (b) Site C, 20-minute averages of data from the periods shown in the prior figure. From left-to-right are along-stream velocity, turbulent stress, and the characteristic (Ellison) turbulent length scale ($L_E \approx 3\sqrt{\tau_{xz}/\rho S^2}$; Stacey et al., 1999a).

Fig. 10: Comparison of stratification (bulk buoyancy frequency, N, for Site B) with the percentage of total turbulence (integrated production) that occurs in the IML (% IML). IML turbulence takes on a relatively larger role during periods of strong stratification.

Fig. 11: At Site C, post-neap transitional tides can have ~15 times higher (lower) IML (BBL) turbulence and mixing than post-spring transitional tides, a hysteresis pattern. The top panel shows the time series of semidiurnal (D2) tidal range, and the two periods shown in the bottom panels are marked with squares and circles for each tidal day, respectively. The lower panels show P_{int} for the bottom boundary layer (BBL) and internal mixing layer (IML). Since the buoyancy flux is roughly proportional to IML P_{int} (Rippeth, 2005), this hysteresis should also exist for the vertical mixing of dissolved constituents.

Table
Click here to download Table: Table1.pdf

Table 1: Cross-correlation analysis summary with maximum positive and negative correlation coefficients (tidal day lag of P_{int} in parentheses), with statistically significant ($\alpha<0.1$) results shaded

P_{int} for:	±r	[a]D2[3]	Q[2]	$U_{wind,1}$[3]	$U_{wind,2}$[3]	bulk N[2]
Site B BBL	+	0.94 (1), α=0.001	0.47 (8), α=0.12	0.22 (-5), α>0.33	0.16 (8), α>0.33	0.65 (7), α>0.33
	-	-0.65 (8), α>0.33	-0.34 (-2), α=0.24	-0.29 (1), α=0.26	-0.15 (-8), α>0.33	-0.84 (-1), α=0.03
Site B IML	+	0.83 (0), α=0.02	0.40 (6), α=0.18	0.24 (-7), α>0.33	0.12 (6), α>0.33	0.64 (7), α=0.18
	-	-0.61 (8), α>0.33	-0.33 (-2), α=0.25	-0.23 (1), α>0.33	-0.09 (-4), α>0.33	–0.69 (–1), α=0.10
Site C BBL	+	0.71 (2), α=0.001	0.52 (8), α=0.08	0.23 (-3), α>0.33	0.31 (8), α=0.19	0.41 (-8), α>0.33
	-	-0.45 (-6), α>0.33	-0.20 (-1), α=0.33	-0.17 (-8), α>0.33	-0.29 (-8), α=0.25	-0.67 (0), α=0.02
Site C IML	+	0.58 (-5), α=0.32	0.56 (0), α=0.06	0.25 (3), α>0.33	0.18 (0), α>0.33	0.81 (1), α<0.001
	-	-0.66 (3), α=0.08	-0.34 (8), α=0.24	-0.50 (-3), α=0.04	-0.31 (8), α=0.19	-0.46 (-7), α>0.33

[a] Positive lags indicate that turbulence (P_{int}) lags behind the driver variable

Figure 1

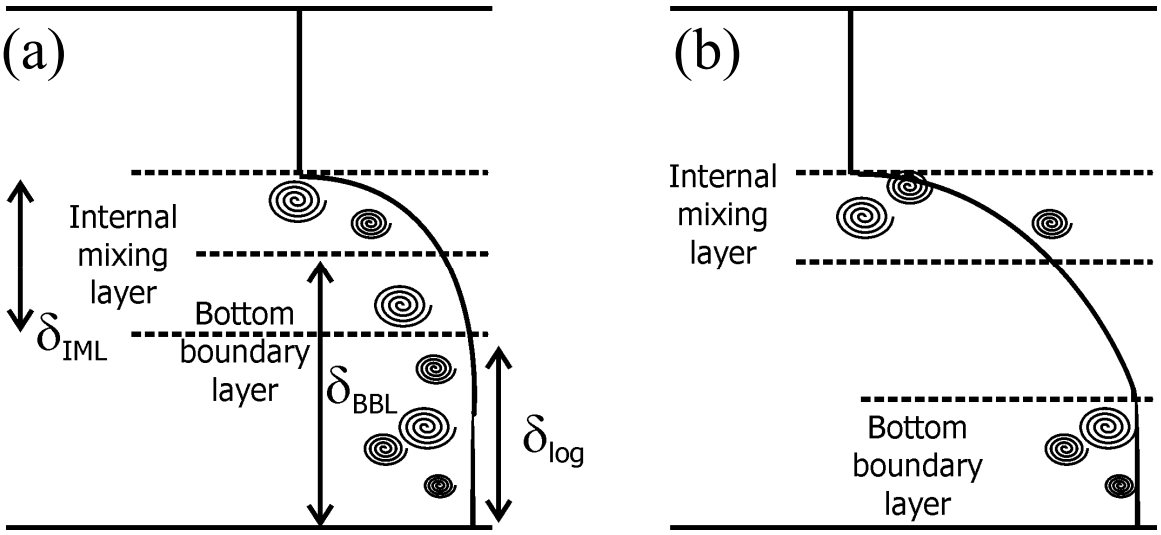

Fig. 1: Conceptual mixing layer diagram with salinity profiles and boundary layer heights (δ). Shown are examples of (a) the case where IML and BBL mixing interact, common in partially mixed estuaries, and (b) the case where the two layers are separate, common in highly stratified estuaries. Adapted from Dyer (1997, p.53).

Figure 2

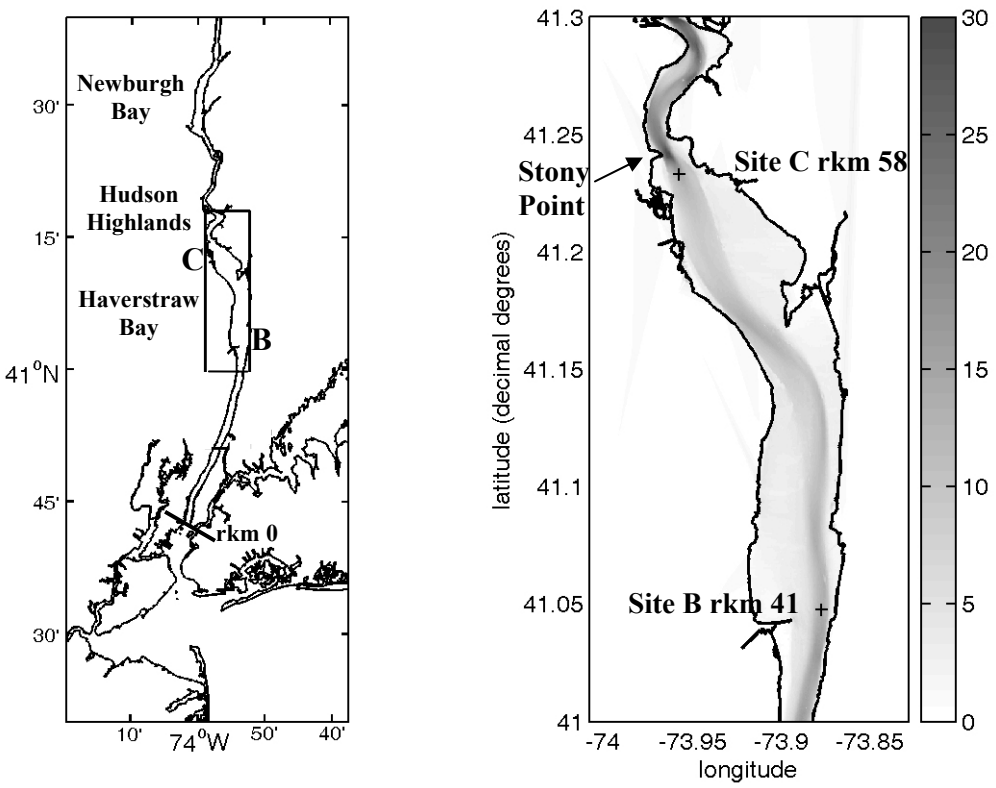

Fig. 2: Hudson River estuary coastline (left) with a zoom-in (right panel) to shaded NOAA-NOS (2006) bathymetry data, and ADCP sites marked '+'. Along-channel distance up-estuary from The Battery (rkm 0 line) is also shown in river kilometers (rkm).

Figure 3

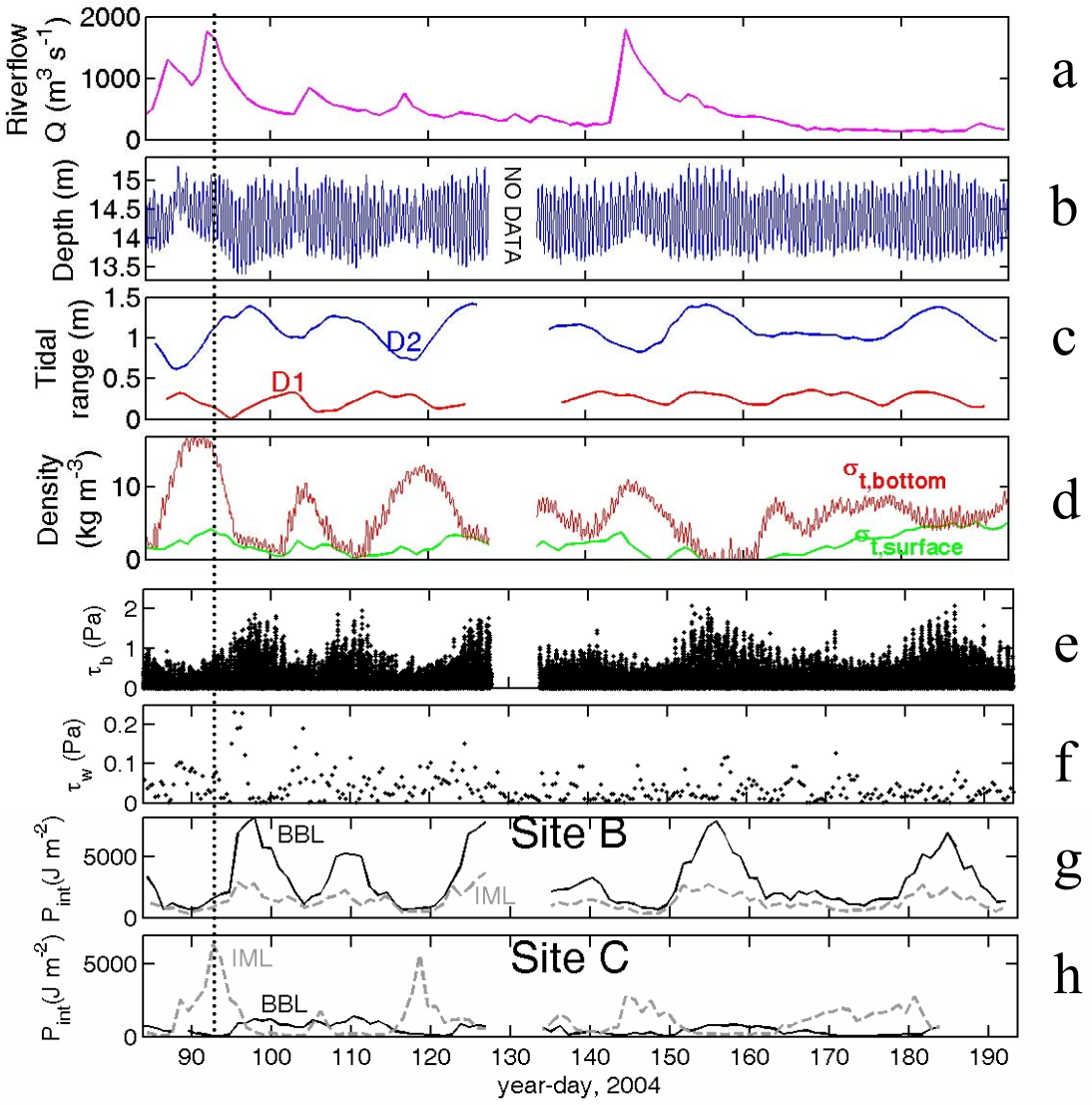

Fig. 3: Time series view of ambient conditions and turbulence variables during the ADCP deployments. Panel (a) shows freshwater input. Panels (b, c and d) show data derived from CTD observations at Site B (0.5 m above the bed), including total depth, semidiurnal (D2) and diurnal (D1) tidal ranges computed with a wavelet transform tidal analysis of depth, water density (σ_t). Panels (e) and (f) show estimates of bed stress (τ_b; **Sec. 3**) at Site B, and wind stress (τ_w). Panels (g) and (h) show integrated turbulent kinetic energy production (P_{int}; **Sec. 3.2**) for the IML and BBL. The dotted vertical line shows the beginning of the year day range for **Fig. 7**.

Figure 4

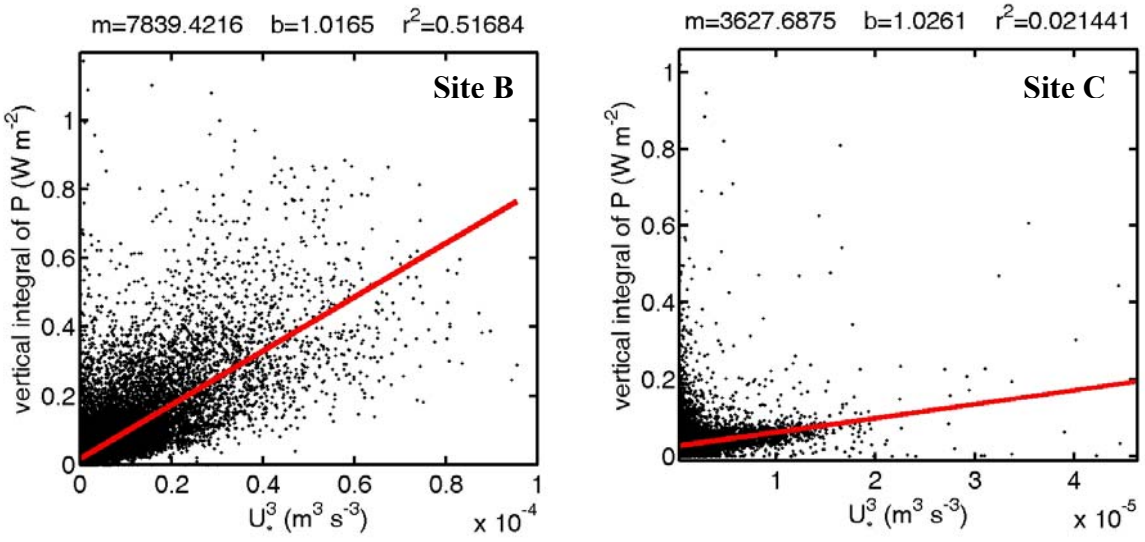

Fig. 4: Relationship between bed frictional forcing (U_*^3) and turbulence (vertically integrated shear production) for Sites B and C. For Site C, there appear to be two distinct regimes, one where turbulence increases with U_*^3, and another where it is strong in spite of low U_*^3.

Figure 5

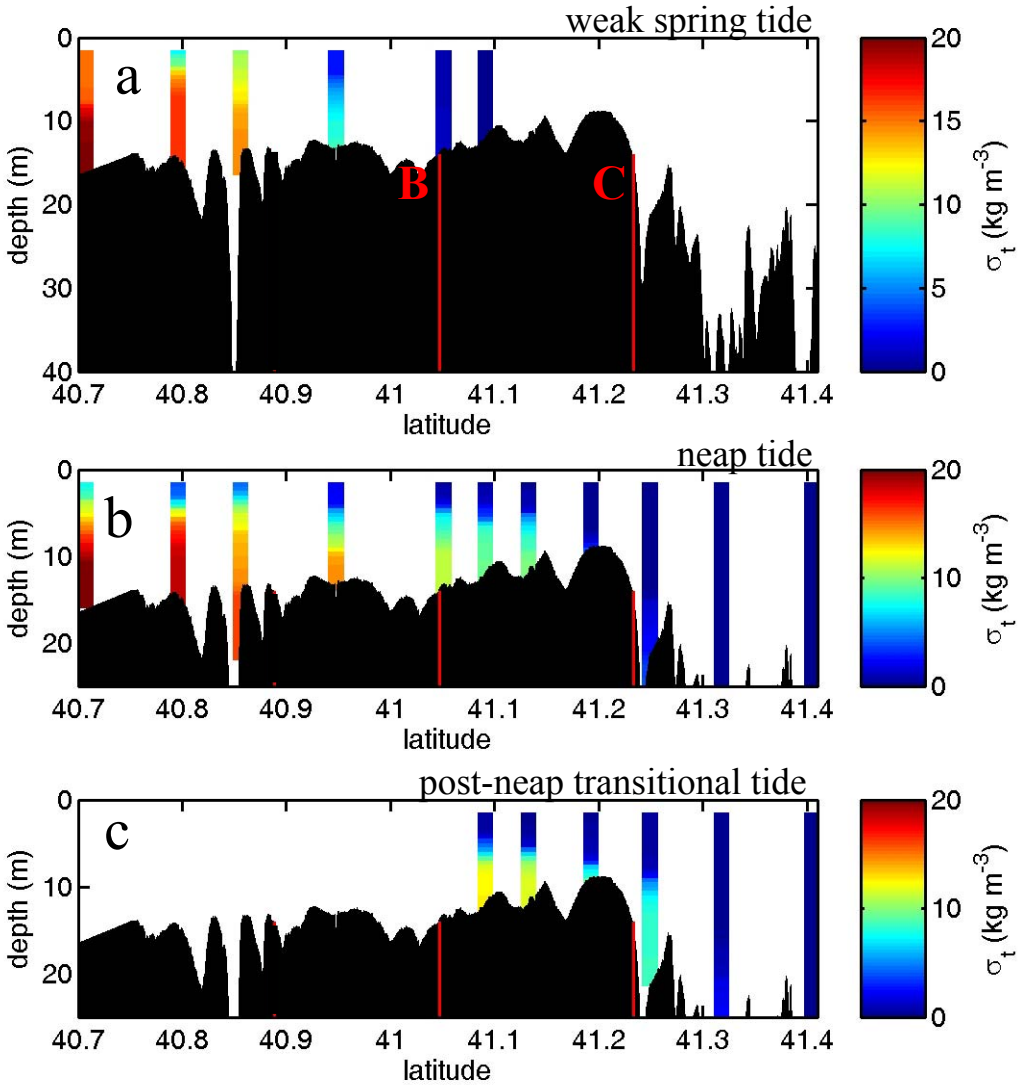

Fig. 5: Three along-channel density transects during spring freshet season, for (a) a weak spring tide (2004 year-day 111, riverflow Q=470 m^3 s^{-1}), (b) one day prior to neap tide (2004 year-day 117, Q=740 m^3 s^{-1}), and three days after neap tide (2005 year-day 108, Q=400 m^3 s^{-1}). Vertical red lines show the ADCP sites, and the thalweg depth is shaded black. The aspect ratio exaggerates bed topography, and actual bed slopes are rarely greater than one percent south of 41.2° N latitude. The salt intrusion length maximum typically lags behind the minimum in tidal forcing, with maximum intrusion length occurring during the post-neap transitional period (see **Sec. 5.3**).

Figure 6

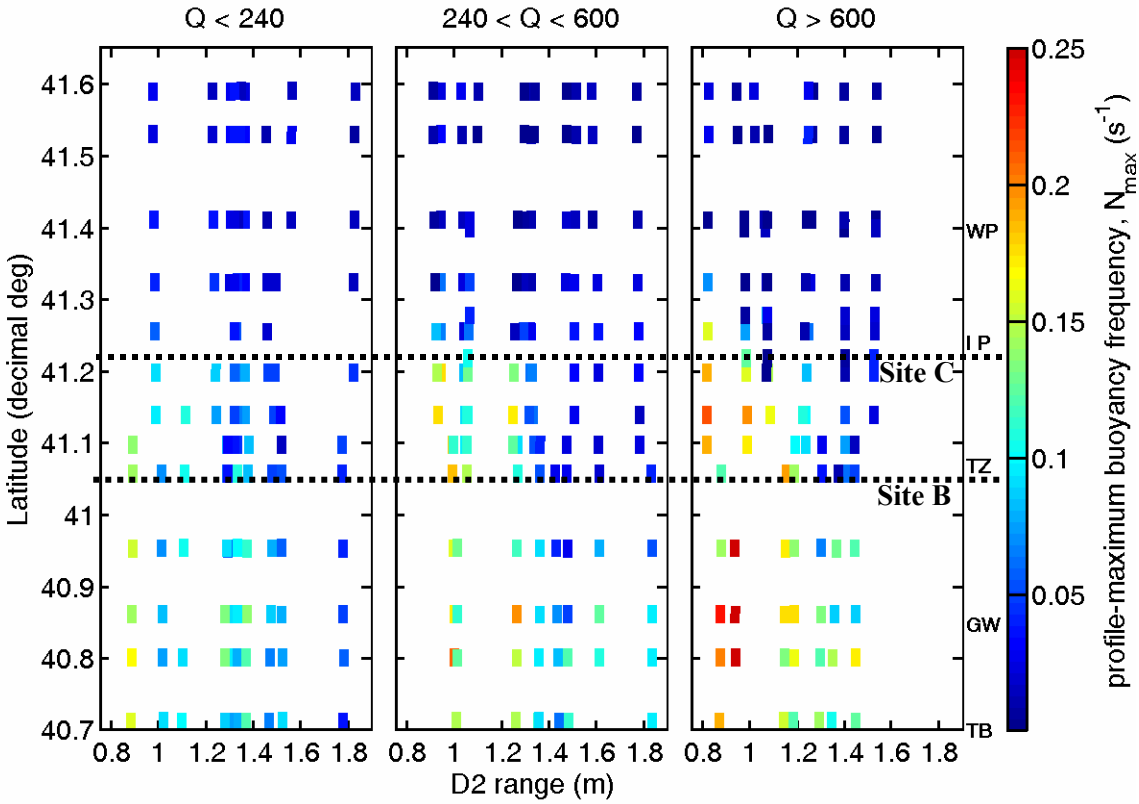

Fig. 6: Summary of stratification (local N) observations the Hudson, with respect to along-channel location (latitude), riverflow (Q; prior 10-day mean) and semi-diurnal (D2; prior 5-day mean) tidal range. The plots summarize data from 30 along-channel transects like those in **Fig. 5**, between 2001 and 2006. Horizontal dotted lines show Sites B and C. Each colored box shows the observed maximum water column stratification from a single profile (from 1.5 m vertical running averages of density). Symbols are (WP) West Point, (IP) Indian Point, (TZ) Tappan Zee Bridge, (GW) George Washington Bridge, and (TB) The Battery.

Figure 7a

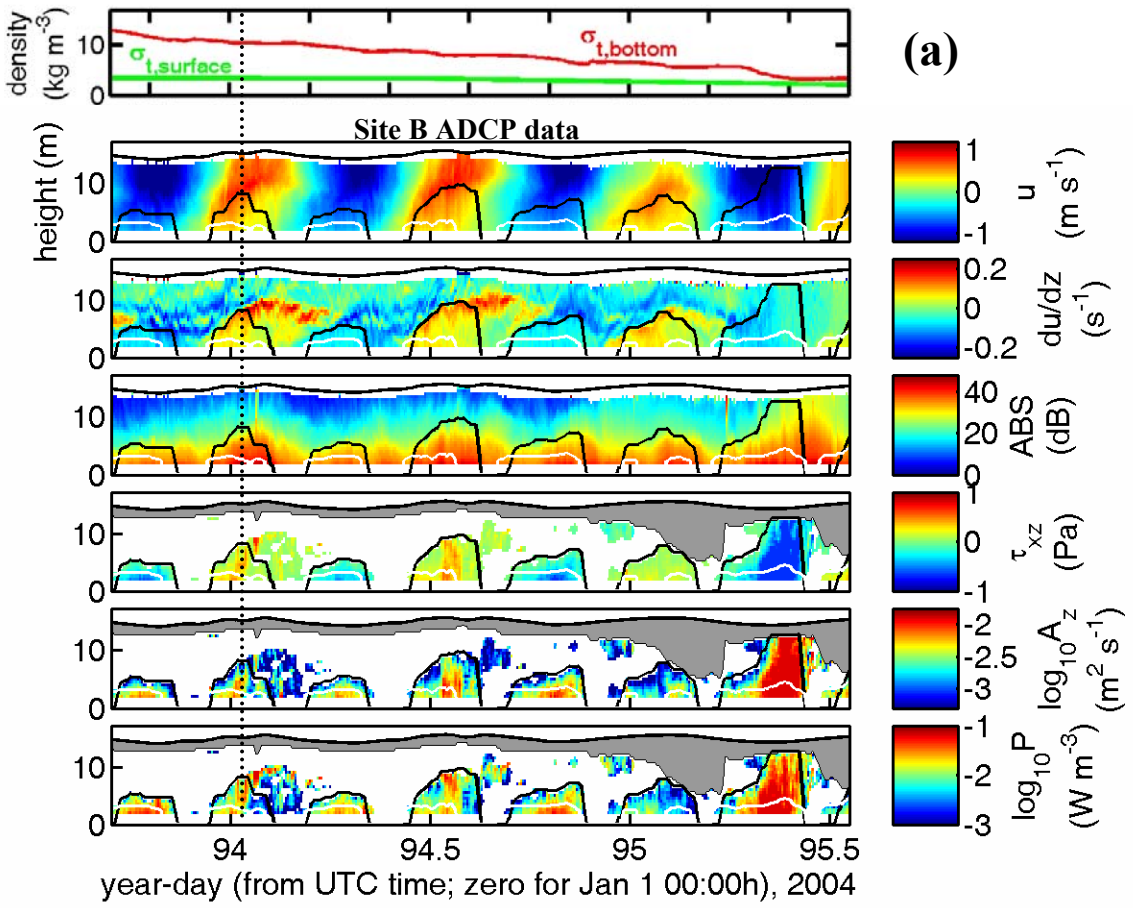

Fig. 7: (a) Site B and (b) Site C zoom-ins of a neap-spring transition with high riverflow. Plotted variables are: density (σ_t), along-stream velocity (u), along-stream vertical shear ($\partial u/\partial z$), acoustic backscatter (ABS), turbulent stress (τ_{xz}), eddy viscosity (A_z), and turbulent kinetic energy production (P). Turbulence data is masked when it is likely dominated by noise (blanked white) or side lobe and wave contamination (grey; see **Sec. 2.2**). The sea surface and bottom boundary layer height (black lines), and log layer height (white line) are shown. The vertical dotted lines show the times for the two figures that follow. Site C exhibits no log layer within our measurement range for most of this period.

Figure 7b

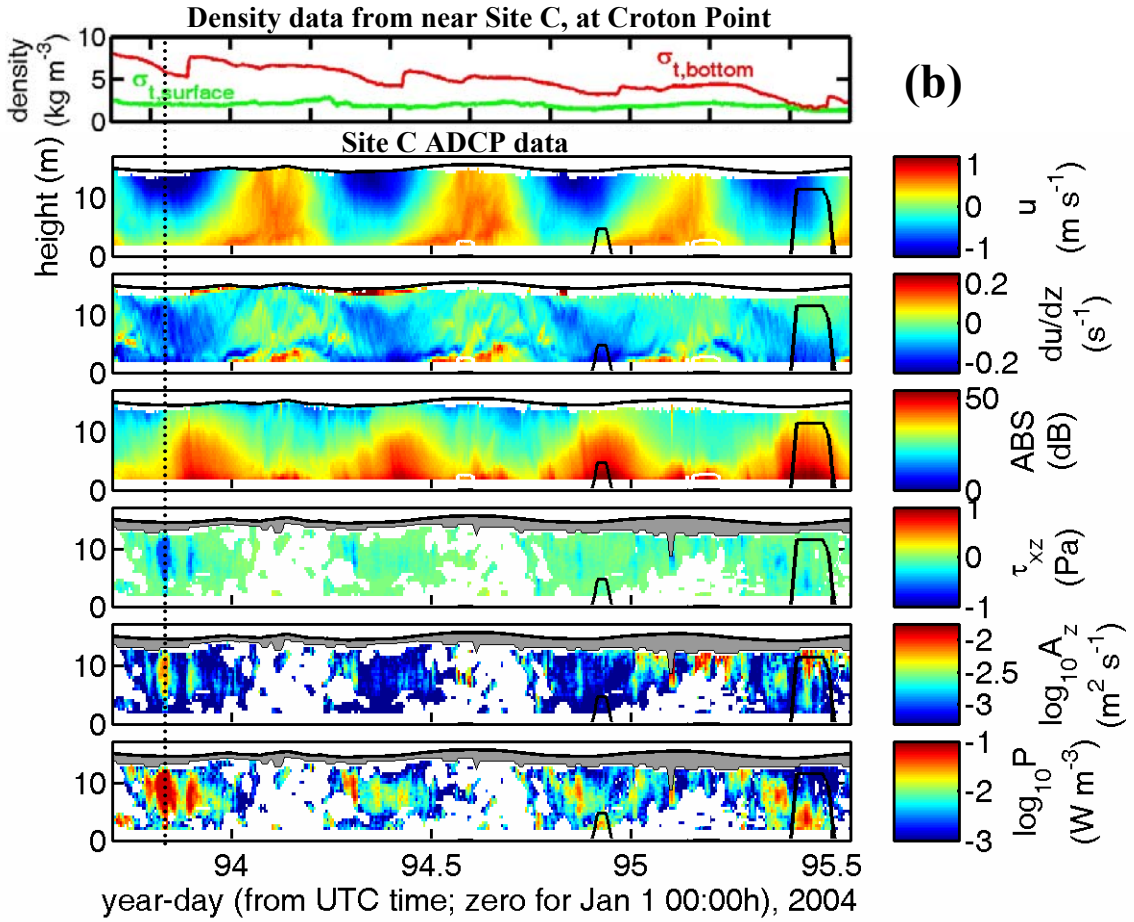

Fig. 7b

Figure 8

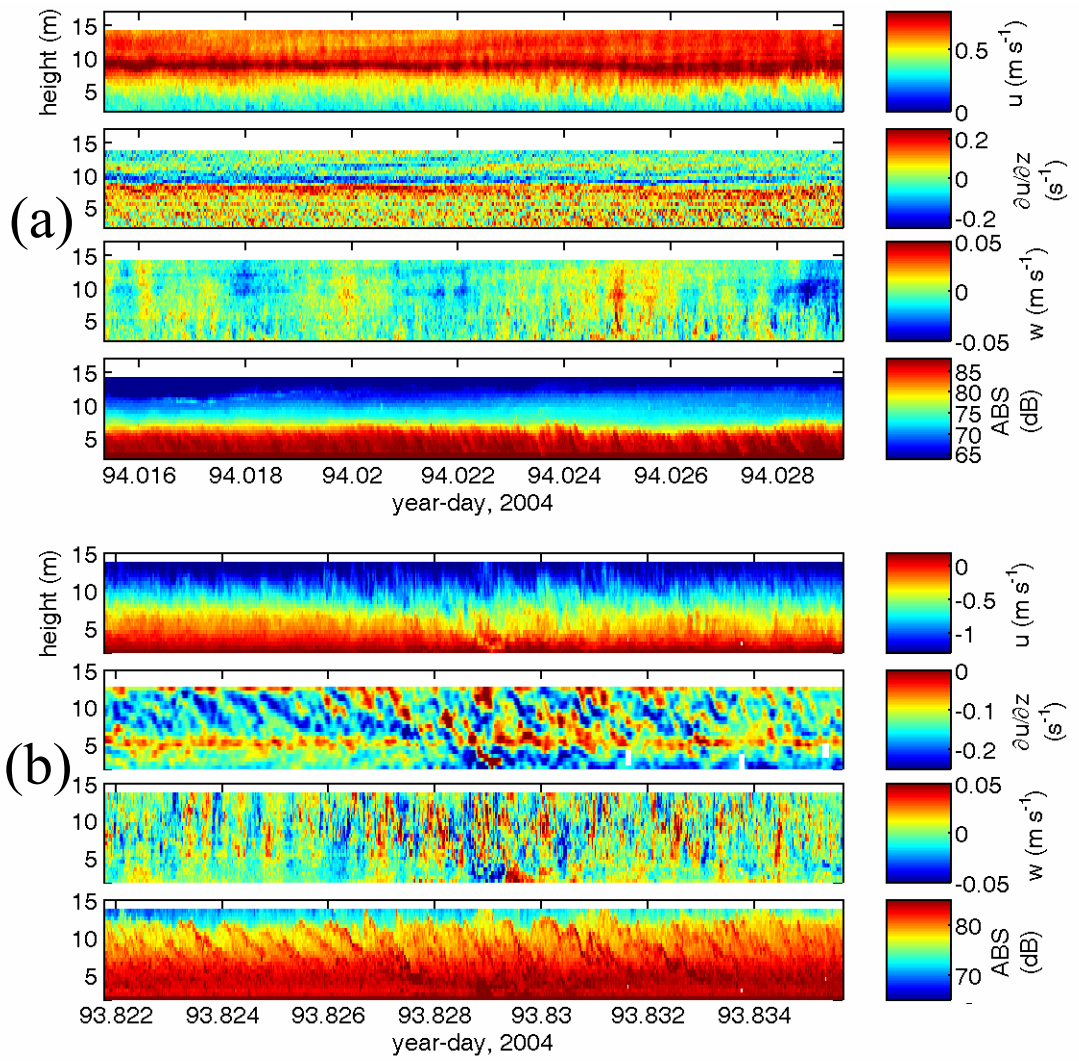

Fig. 8: Zoom-ins to 0.5 Hz raw data for 20-minute periods at (a) Site B, and (b) Site C. Shown are: along-stream velocity (u), vertical shear (∂u/∂z), vertical velocity (w), and acoustic backscatter from a single ADCP beam (ABS). For Site C, shear is box-filtered with a 1.5 m by 10 s window, due to excessive variability. The following plot shows averaged turbulent stress profiles from these periods.

Figure 9

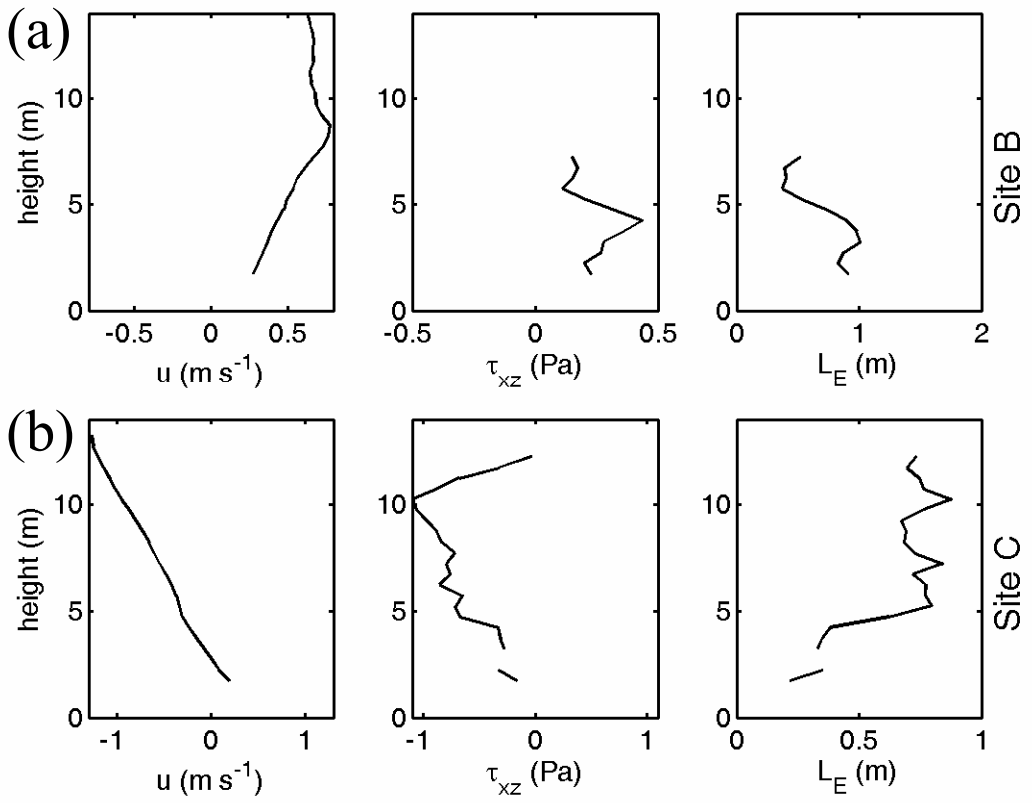

Fig. 9: (a) Site B and (b) Site C, 20-minute averages of data from the periods shown in the prior figure. From left-to-right are along-stream velocity, turbulent stress, and the characteristic (Ellison) turbulent length scale ($L_E \approx 3\sqrt{\tau_{xz}/\rho S^2}$; Stacey et al., 1999a).

Figure 10

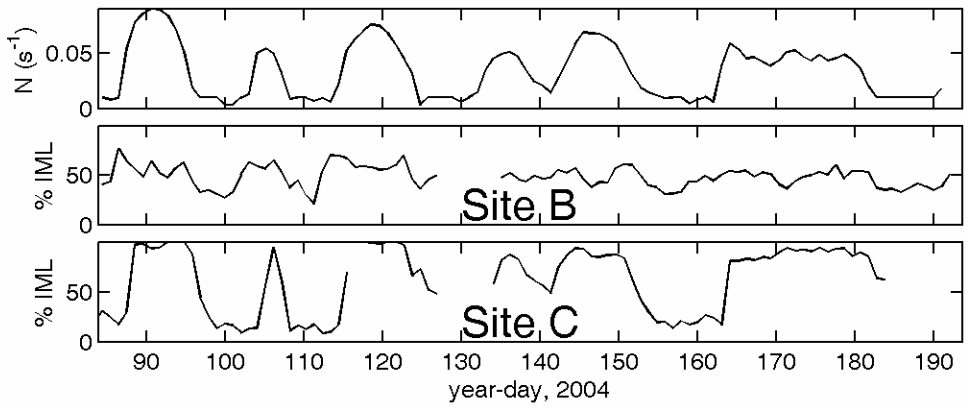

Fig. 10: Comparison of stratification (bulk buoyancy frequency, N, for Site B) with the percentage of total turbulence (integrated production) that occurs in the IML (% IML). IML turbulence takes on a relatively larger role during periods of strong stratification.

Figure 11

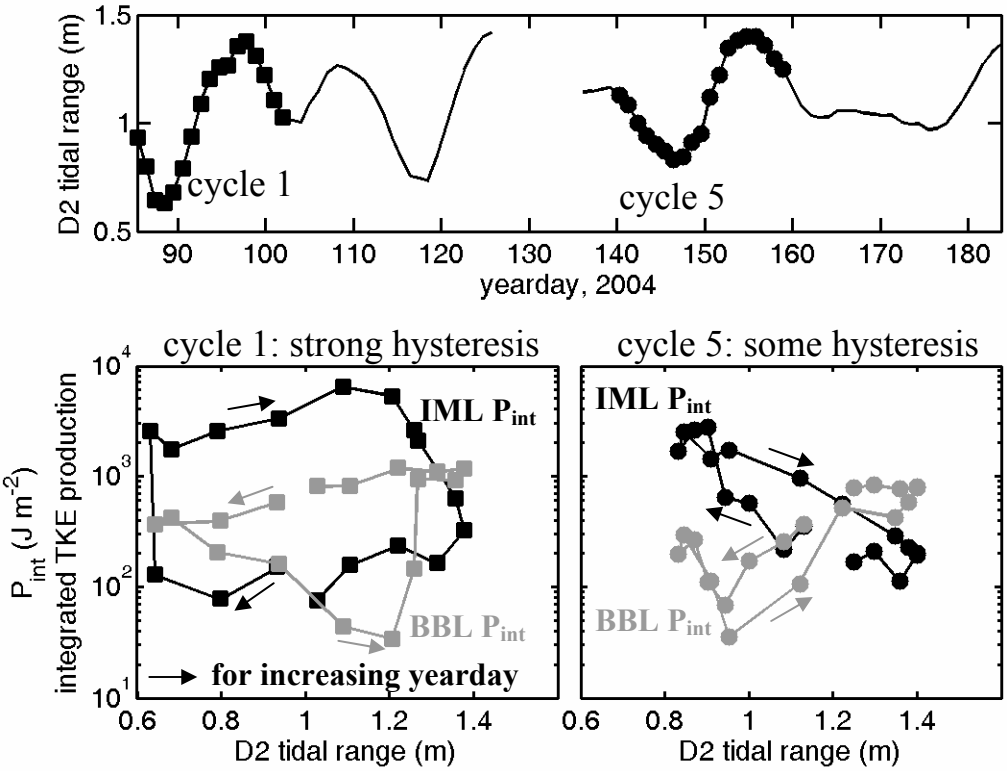

Fig. 11: At Site C, post-neap transitional tides can have ~15 times higher (lower) IML (BBL) turbulence and mixing than post-spring transitional tides, a hysteresis pattern. The top panel shows the time series of semidiurnal (D2) tidal range, and the two periods shown in the bottom panels are marked with squares and circles for each tidal day, respectively. The lower panels show P_{int} for the bottom boundary layer (BBL) and internal mixing layer (IML). Since the buoyancy flux is roughly proportional to IML P_{int} (Rippeth, 2005), this hysteresis should also exist for the vertical mixing of dissolved constituents.